On the Robustness and Efficiency of the Plane-Wave-Enriched FEM with Variable q-Approach on the 2D Room Acoustics Problem

Mukae, Shunichi
Okuzono, Takeshi
Sakagami, Kimihiro

acoustics

MDPI

Article

On the Robustness and Efficiency of the Plane-Wave-Enriched FEM with Variable *q*-Approach on the 2D Room Acoustics Problem

Shunichi Mukae [1], Takeshi Okuzono [1,*] and Kimihiro Sakagami [1]

Environmental Acoustics Laboratory, Department of Architecture, Graduate School of Engineering, Kobe University, Kobe 657-8501, Japan; shun.giants0324@gmail.com (S.M.); saka@kobe-u.ac.jp (K.S.)
* Correspondence: okuzono@port.kobe-u.ac.jp; Tel.: +81-78-803-6577

Abstract: Partition of unity finite element method with plane wave enrichment (PW-FEM) uses a shape function with a set of plane waves propagating in various directions. For room acoustic simulations in a frequency domain, PW-FEM can be an efficient wave-based prediction method, but its practical applications and especially its robustness must be studied further. This study elucidates PW-FEM robustness via 2D real-scale office room problems including rib-type acoustic diffusers. We also demonstrate PW-FEM performance using a sparse direct solver and a high-order Gauss–Legendre rule with a recently developed rule for ascertaining the number of integration points against the classical linear and quadratic FEMs. Numerical experiments investigating mesh size and room geometrical complexity effects on the robustness of PW-FEM demonstrated that PW-FEM becomes more robust at wide bands when using a mesh in which the maximum element size maintains a comparable value to the wavelength of the upper-limit frequency. Moreover, PW-FEM becomes unstable with lower spatial resolution mesh, especially for rooms with complex shape. Comparisons of accuracies and computational costs of linear and quadratic FEM revealed that PW-FEM requires twice the computational time of the quadratic FEM with a mesh having spatial resolution of six elements per wavelength, but it is highly accurate at wide bands with lower memory and with markedly fewer degrees of freedom. As an additional benefit of PW-FEM, the impulse response waveform of quadratic FEM in a time domain was found to deteriorate over time, but the PW-FEM waveform can maintain accurate waveforms over a long time.

Keywords: acoustic simulation; architectural acoustics; finite element method; wave-based modeling

Citation: Mukae, S.; Okuzono, T.; Sakagami, K. On the Robustness and Efficiency of the Plane-Wave-Enriched FEM with Variable *q*-Approach on the 2D Room Acoustics Problem. *Acoustics* **2022**, *4*, 53–73. https://doi.org/10.3390/acoustics4010004

Academic Editor: Claudio Guarnaccia

Received: 15 December 2021
Accepted: 12 January 2022
Published: 20 January 2022

1. Introduction

1.1. Background

Numerical simulations of room acoustics are a useful tool for designing a comfortable sound environment in various architectural spaces such as offices and classrooms. Geometrical acoustics simulation methods [1] such as the ray tracing method are practical and powerful room acoustics simulation tools with low computational resources. However, they use a simplified approximation of wave phenomena. Wave-based numerical methods such as finite element methods (FEMs) can predict room acoustics accurately by solving a wave equation numerically. The wave-based methods have a notable benefit in modeling two major technologies for room acoustics control, i.e., the effect of sound absorption and sound scattering can be considered more precisely. Nevertheless, they require a high computational cost for predicting a great variety of sound fields of real-scale architectural spaces with complex boundary conditions at wide ranges of audible frequencies. They entail fine discretization in time and space to maintain a discretization error, known as the dispersion error, within an acceptable level. In general, the classical linear and quadratic FEMs respectively require spatial discretization of at least 10 and 3 elements per wavelength as a rule of thumb for spatial discretization. These discretization rules,

which increase the degrees of freedom in FE meshes, make the room acoustics problem considerably expensive. However, with recent developments in computer technology and efficient solvers, the applicable range of wave-based numerical methods is progressing rapidly for both frequency-domain and time-domain room acoustic simulations [2–5]. For frequency-domain room acoustics simulation, FEM [6–9] and the boundary element method [10,11] are standard choices because they can model various sound absorbers more easily than time-domain methods can. In contrast, with the capability of obtaining the impulse response with a single computational run, the following time-domain room acoustic simulations have been developed: the finite-difference time-domain method [12–16], the time-domain FEM [3,17–19], the finite-volume time-domain method [20,21], the pseudospectral time-domain method [22,23], the discontinuous Galerkin FEM [24–27], and the adaptive rectangular decomposition method [28,29]. However, acoustics simulation in a real-sized room at high frequencies must address analytical models with vast degrees of freedom (DOFs). Consequently, developing more efficient methods has a marked effect on enhancing of their applicability further in practical room acoustics design.

As such a candidate, the authors expect that the partition of unity FEM [30–42] with plane-wave enrichment (PW-FEM) can be an effective method from the perspectives of accuracy, efficiency, ease of mesh generation, and compatibility with existing FEM codes. Actually, PW-FEM is extendable from any existing FEM code, i.e., the method is inherently helpful for the performance enhancement of existing FEM codes. In the PW-FEM and relevant methods such as the partition of unity isogeometric analysis, the sound pressure at each node is represented by a sum of plane waves propagating in various directions, using a general solution of the Helmholtz equation. With the incorporation of the plane wave function, the PW-FEM can enhance the approximation capability of sound fields [32,33,35,36]. Furthermore, using a refinement approach called q-refinement by which a set of plane waves is added gradually at nodal points, the PW-FEM can approximate sound fields up to high frequencies under a single coarse mesh discretized with elements of length many times greater than the wavelength of the analyzed frequency. Consequently, the PW-FEM can reduce the DOFs markedly compared to the classical linear FEM. Our recent research [37] assessing the potential of the PW-FEM as an efficient room acoustics solver via two room-acoustic problems showed that the DOFs' reduction reaches at least 1/100 compared to the classical linear FEM. Furthermore, the authors proposed a new rule for ascertaining the number of integration points in the high-order Gauss–Legendre rule used for the construction of element matrices [40], which is known as a hotspot of computations, and demonstrated its efficiency for wideband frequency response analysis against the well-used existing rule. Then, the authors presented the applicability of the PW-FEM to room acoustics simulation, including an extended reacting microperforated panel [43] and permeable membrane [44] sound absorbers in the literature [42]. We can also find appropriate PW-FEM formulations for predicting sound fields including porous sound absorbers [38,39], for which porous materials are modelled with an equivalent fluid model [45–48] and poroelastic material model [49].

However, there is still an unclear and difficult point for users in the parameter setup on the plane-wave enrichment. That point is associated with the robustness of the PW-FEM and becomes an error factor. At present, a well-used rule as a function of wavenumber and element size exists for plane-wave enrichment, which includes a constant to control accuracy. However, its robustness on the room acoustics problem remains unclear. Because the room acoustics problems include elements of multiple sizes in FE meshes according to the room geometry and need multi-frequency analysis, it is crucially important to find a robust mode of adding appropriate numbers of plane waves to nodal points according to the mesh, frequency, and room geometry. For example, one must use a PW-FE mesh that includes both smaller and larger elements compared to the wavelength of the analyzed frequency when a room includes acoustic diffusers for room acoustics control.

1.2. Study Purpose

This study was conducted to investigate how the robustness of PW-FEM in multi-frequency analysis changes according to the mesh and room geometry which are used. Based on the results, the authors present a proposal for the mesh used to perform room acoustics simulations efficiently with PW-FEM. This paper also includes performance examination in terms of computational times and memory requirements against standard linear and quadratic FEMs. The PW-FEM uses our recently developed rule for ascertaining the number of integration points in the high-order Gauss–Legendre rule and uses a sparse direct solver for linear system solutions. The two standard FEMs also use the sparse direct solver. As the main contribution to the earlier works, this report is the first to describe the robustness of PW-FEM for application to room acoustics problems and to show performance over standard FEMs when using a sparse direct solver. Note that the present paper specifically addresses 2D room acoustics problems. However, the presented formulation using our recently developed rule in the high-order Gauss–Legendre rule and the proposal on mesh generation would be a good foundation for constructing robust and efficient 3D room acoustics solver using PW-FEM. Furthermore, we expect that the presented 2D PW-FEM would be helpful as a rough room acoustics design tool at an early stage of acoustics design, such as examining room shapes and placement of sound absorbers and acoustic diffusers, with higher accuracy than linear and quadratic FEMs.

The remainder of this study is organized as explained below. First, we describe the theory of the PW-FEM for the readers' convenience. Then, we conducted three numerical experiments. As a fundamental investigation, we first present the effectiveness of a mode of plane-wave enrichment called the Variable q-approach for room acoustics simulation using a mesh consisting of various sized elements compared to another mode called the Constant q-approach via numerical experiments predicting sound fields in a real-scale office room with a rib-type acoustic diffuser. The second numerical experiment investigates the effects of the spatial resolution of used mesh and room geometry on the robustness of the PW-FEM in multi-frequency analysis. Finally, we present the performance of the PW-FEM against the classical linear and quadratic FEMs. The discussion in this paper is limited to cases using a high-order Gauss–Legendre rule for element matrices' construction, as shown in Section 2, because it is the general approach able to use any type of FEs. However, analytical integration schemes have been studied to enhance the efficiency of the PW-FEM when using a mesh discretized with larger elements than the wavelength of the analyzed frequencies. For readers interest in the analytical integration schemes, earlier reports of the literature [50,51] are useful.

2. Theory

2.1. Discretization of the Closed Sound Field Using Plane-Wave-Enriched FEM

We considered a sound propagation problem in a closed sound field Ω with boundary Γ governed by the following Helmholtz equation in terms of sound pressure p at the wavenumber in air k_0 as shown below:

$$\nabla^2 p + k_0^2 p = 0 \quad \text{in } \Omega. \tag{1}$$

The boundary Γ is composed of three boundary conditions (BCs): a rigid BC Γ_0, a vibration BC Γ_v, and an absorbing BC Γ_z. They are respectively described as:

$$\frac{\partial p}{\partial n} = \begin{cases} 0 & \text{on } \Gamma_0 \\ -\mathrm{j}\omega\rho_0 v_\mathrm{n} & \text{on } \Gamma_\mathrm{v} \\ -\mathrm{j}k_0 Y_\mathrm{n} p & \text{on } \Gamma_\mathrm{z} \end{cases}, \tag{2}$$

where j, ω, ρ_0, v_n, and Y_n respectively represent the imaginary unit, the angular frequency, the air density, the vibration velocity, and the specific acoustic admittance ratio. Note that Y_n introduces the sound absorption effect of materials. One can use theoretical calculation by the transfer matrix method or impedance tube measurements to obtain Y_n of porous

and Helmholtz type sound absorbers. The following equation is also available when using real-valued Y_n as a simple absorption treatment.

$$Y_\mathrm{n} = \left(\frac{1+\sqrt{1-\alpha_0}}{1-\sqrt{1-\alpha_0}} \right)^{-1}, \tag{3}$$

where α_0 is the normal incidence sound absorption coefficient. The weak form of the Helmholtz equation for plane-wave-enriched FEM is:

$$\int_\Omega (-\nabla\phi\nabla p + k_0^2\phi p)\,\mathrm{d}\Omega + \int_\Gamma \phi\frac{\partial p}{\partial n}\,\mathrm{d}\Gamma = 0, \tag{4}$$

where ϕ denotes the arbitrary weight function. A classical FEM approximates sound pressure at an arbitrary point $p(x,y)$ within an element Ω_e as:

$$p(x,y) = \sum_{i=1}^{n} N_i(\xi,\eta) p_i^{\Omega_\mathrm{e}} \quad \text{in } \Omega_\mathrm{e}, \tag{5}$$

where $N_i(\xi,\eta)$ and $p_i^{\Omega_\mathrm{e}}$ respectively represent the shape function in two-dimensional local coordinates (ξ,η) and nodal sound pressure. The present paper used the following Lagrange polynomials for $N_i(\xi,\eta)$ as:

$$L_a(\xi) = \prod_{b=1,(b\neq a)}^{p^\xi+1} \frac{\xi-\xi_b}{\xi_a-\xi_b}. \tag{6}$$

The Lagrange polynomial $L_a(\xi)$ above represents a function form for the ξ direction, in which a is the node location, ξ_a is their local coordinate, $p^\xi+1$ is the node number used for approximation, and p^ξ is the order of the polynomial. By application of this expression to the η direction, the shape function $N_i(\xi,\eta)$ for quadrilateral elements is given as:

$$N_i(\xi,\eta) = L_a(\xi)L_a(\eta). \tag{7}$$

The present paper uses four-node quadrilateral elements (Q4s) with the polynomial order of $p^\xi = p^\eta = 1$ for the PW-FEM, and Q4s and nine-node quadrilateral elements (Q9s) with $p^\xi = p^\eta = 2$ for linear and quadratic FEMs.

Actually, PW-FEM further approximates nodal sound pressure $p_i^{\Omega_\mathrm{e}}$ with the plane-wave enrichment. That is, $p_i^{\Omega_\mathrm{e}}$ is approximated by a sum of plane waves propagating in various directions as:

$$p_i^{\Omega_\mathrm{e}} = \sum_{l=1}^{q_i} \mathrm{e}^{\mathrm{j}k_0(x\cos\theta_l + y\sin\theta_l)} A_i^l, \tag{8}$$

where q_i, θ_l, and A_i^l respectively represent the number of plane waves added at node i, the angles of the plane waves, and the amplitude of the plane waves propagating in a direction θ_l. The method of determining the adding number of plane waves is explained later. With Equations (5) and (8), the PW-FEM approximates $p(x,y)$ within an element as:

$$p(x,y) = \sum_{i=1}^{n}\sum_{l=1}^{q_i} N_i(\xi,\eta)\mathrm{e}^{\mathrm{j}k_0(x\cos\theta_l + y\sin\theta_l)} A_i^l = \boldsymbol{P}\boldsymbol{a}_\mathrm{e} \quad \text{in } \Omega_\mathrm{e}, \tag{9}$$

where $\boldsymbol{a}_\mathrm{e}$ is the element amplitude vector. The vector $\boldsymbol{P} = (P_1, P_2, \cdots, P_m, \cdots, P_{q_\mathrm{tot}^{\Omega_\mathrm{e}}})$ is a new shape function vector constructed from the new shape function P, which is expressed as:

$$P_m(\xi,\eta) = N_i(\xi,\eta)\mathrm{e}^{\mathrm{j}k_0(x\cos\theta_l + y\sin\theta_l)}, \tag{10}$$

with:

$$m = (\sum_{i=1}^{i} q_i) - q_i + l, \tag{11}$$

$$q_{\mathrm{tot}}^{\Omega_\mathrm{e}} = \sum_{i \in \Omega_\mathrm{e}} q_i. \tag{12}$$

Inserting the three BCs given by Equation (2) and the PW-FE approximation in Equation (9) into the weak form of the Helmholtz equation in Equation (4), one can obtain the following linear system of equations with the sparse coefficient matrix expressed as:

$$[\boldsymbol{K} - k_0^2 \boldsymbol{M} + \mathrm{j}k_0 \boldsymbol{C}]\boldsymbol{A} = -\mathrm{j}\omega\rho_0 \boldsymbol{Q}, \tag{13}$$

with:

$$\boldsymbol{K} = \sum_\mathrm{e} \boldsymbol{k}_\mathrm{e} = \sum_\mathrm{e} \int_{\Omega_\mathrm{e}} (\nabla \boldsymbol{P})^\mathrm{T} \nabla \boldsymbol{P} \mathrm{d}\Omega_\mathrm{e}, \tag{14}$$

$$\boldsymbol{M} = \sum_\mathrm{e} \boldsymbol{m}_\mathrm{e} = \sum_\mathrm{e} \int_{\Omega_\mathrm{e}} \boldsymbol{P}^\mathrm{T} \boldsymbol{P} \mathrm{d}\Omega_\mathrm{e}, \tag{15}$$

$$\boldsymbol{C} = \sum_\mathrm{e} \boldsymbol{c}_\mathrm{e} = \sum_\mathrm{e} Y_\mathrm{n} \int_{\Gamma_{\mathrm{e},z}} \boldsymbol{P}^\mathrm{T} \boldsymbol{P} \mathrm{d}\Gamma_\mathrm{e}, \tag{16}$$

$$\boldsymbol{A} = \sum_\mathrm{e} \boldsymbol{a}_\mathrm{e}, \tag{17}$$

$$\boldsymbol{Q} = \sum_\mathrm{e} \boldsymbol{q}_\mathrm{e} = \sum_\mathrm{e} v_\mathrm{n} \int_{\Gamma_{\mathrm{e},v}} \boldsymbol{P}^\mathrm{T} \mathrm{d}\Gamma_\mathrm{e}. \tag{18}$$

Here, $\boldsymbol{K}$, $\boldsymbol{M}$, and $\boldsymbol{C}$ respectively represent the global stiffness matrix constructed from an element matrix $\boldsymbol{k}_\mathrm{e}$, the global mass matrix constructed from element mass matrix $\boldsymbol{m}_\mathrm{e}$, and the global dissipation matrix constructed from element dissipation matrix $\boldsymbol{c}_\mathrm{e}$. Also in that equation, $\boldsymbol{A}$ and $\boldsymbol{Q}$ respectively denote the nodal amplitude vector constructed from element amplitude vector $\boldsymbol{a}_\mathrm{e}$ and the external force vector constructed from element external force vector $\boldsymbol{q}_\mathrm{e}$. The domain and boundary integrals in the element matrix constructions are calculated using high-order Gauss–Legendre rules. As an example, $\boldsymbol{k}_\mathrm{e}$ is calculated as:

$$\boldsymbol{k}_\mathrm{e} = \sum_{i=1}^{n_\mathrm{g}} \sum_{j=1}^{n_\mathrm{g}} \omega_i \omega_j (\nabla \boldsymbol{P}(\xi_i, \eta_j))^\mathrm{T} \boldsymbol{P}(\xi_i, \eta_j) \det(\boldsymbol{J}), \tag{19}$$

where ω_i and ω_j respectively stand for weights at the integration points (ξ_i, η_j) and where $\det(\boldsymbol{J})$ denotes the determinant of the Jacobian matrix $\boldsymbol{J}$. The number of integration points n_g is determined by the following recently developed equation [40] depending on the analyzed frequency and element size as:

$$n_\mathrm{g} = \mathrm{int}(5n_\mathrm{w} + 6), \tag{20}$$

where the function int() represents the conversion to an integer by rounding down and n_w is the ratio of wavelength λ to the longest edge length in each element $h_{\mathrm{max}}^{\Omega_\mathrm{e}}$, i.e., $n_\mathrm{w} = h_{\mathrm{max}}^{\Omega_\mathrm{e}}/\lambda$. Using the high-order Gauss–Legendre rule with Equation (20), one can analyze the frequency response at a wide frequency range faster than the rule that is often used, i.e., $n_\mathrm{g} = \mathrm{int}(10n_\mathrm{w} + 1)$ for high frequencies, while maintaining the accuracy because of the reduced number of integration points n_g.

Finally, complex sound pressure in the domain Ω is calculated by substituting A_i^l obtained from Equation (13) into Equation (9). The present study used a sparse direct solver called PARDISO (included in Intel Math Kernel Library) to solve the linear system of equations of Equation (13). The coefficient matrix is stored using a sparse storage format, namely the compressed row storage format.

2.2. Setup of the Plane-Wave Number for q-Refinement

The PW-FEM performs multi-frequency analysis under a single mesh using a q-refinement approach, by which the added plane-wave number increases gradually according to the analyzed frequencies. This paper used the following methods for ascertaining how many plane waves add to the nodal points in a PW-FEM mesh [34,37,39] as:

$$q_i = \text{round}\left[k_0 h^{\Omega}_{\max} + C(k_0 h^{\Omega}_{\max})^{\frac{1}{3}}\right], \tag{21}$$

$$q_i = \text{round}\left[k_0 h^{\Omega}_{\max,i} + C(k_0 h^{\Omega}_{\max,i})^{\frac{1}{3}}\right], \tag{22}$$

where $h^{\Omega}_{\max}$ and $h^{\Omega}_{\max,i}$ respectively denote the longest edge length in all elements and the longest edge length connected to node i. The constant C adjusts the resulting accuracy, but no established method exists to set an appropriate value of C in advance. We designate the approach with Equation (21) as the Constant q-approach because the numbers of added plane waves are constant at all nodal points. We designate the approach with Equation (22) as the Variable q-approach, which uses variable numbers of added plane waves according to the edge length connected to node i. Figure 1a,b present examples of the difference of q-refinement using the Constant q- and Variable q-approach under a mesh consisting of four elements discretized with a 0.1 m × 0.1 m square element, two 0.5 m × 0.1 m rectangular elements, and a 0.5 m × 0.5 m square element. Note that the total DOFs q^{Ω}_{tot} in the PW-FE mesh with both approaches can be calculated by $q^{\Omega}_{\text{tot}} = \sum_{i\in\Omega} q_i$, and q^{Ω}_{tot} becomes smaller for the Variable q-approach, as in Figure 1a,b.

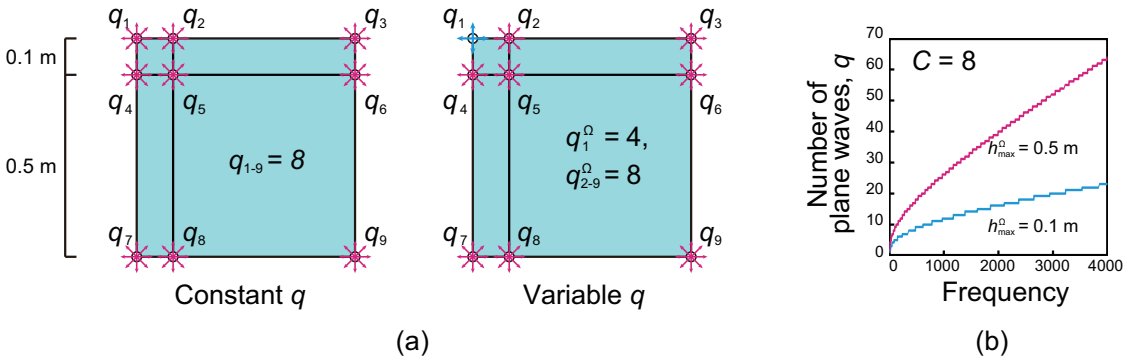

Figure 1. An example of q-refinement using the Constant q- and Variable q-approach: (**a**) the difference between Constant q and Variable q in the element patch composed of a 0.1 m × 0.1 m square element, two 0.5 m × 0.1 m rectangular elements, and a 0.5 m × 0.5 m square element; (**b**) the change in the adding plane-wave number in the Variable q-approach at frequencies up to 4 kHz for the case with C = 8 when using $h^{\Omega}_{\max,i}$ = 0.5 m and 0.1 m.

3. Numerical Experiments

This section presents an assessment of the robustness and efficiency of the PW-FEM with Variable q-approach via a 2D real-scale office room problem with a rib-type acoustic diffuser, at frequencies up to 4 kHz. As a basic investigation, Section 3.2 clarifies the effectiveness of the Variable q-approach against the Constant q-approach. Section 3.3 shows mesh size and room geometry effects on the PW-FEM robustness using two models with different geometrical complexities and three meshes with different spatial resolutions. Finally, in Section 3.4, we show the efficiency of the PW-FEM with Variable q-approach through the performance comparison against the classical linear and quadratic FEMs. Note that all computational codes used in the present study are written by Fortran 90 programing language.

3.1. Problem Description and Numerical Setup

Figure 2a,b presents the office room models with different geometrical complexities: Model A in Figure 2a includes a rib-type acoustic diffuser, and Model B in Figure 2b, which has a simpler room shape, and which does not include the diffuser. We used Model B only in Section 3.3 for revealing the room geometry effect on the robustness. The two models have three BCs comprising a weakly absorbing boundary $\Gamma_{z,1}$, an absorbing boundary $\Gamma_{z,m}$, and a vibration boundary Γ_v. The weakly absorbing boundary $\Gamma_{z,1}$ has a real-valued impedance corresponding to the normal incidence absorption coefficient of $\alpha_0 = 0.05$. The absorbing boundary $\Gamma_{z,m}$ assumes a honeycomb-backed microperforated panel (MPP) absorber with the following geometrical parameters: 0.5 mm hole diameter, 1 mm panel thickness, 0.75% perforation ratio, 1.13 kg/m^2 surface density, and 0.015 m backing honeycomb core depth. The absorption characteristics of the MPP absorber computed using the theory [9] are also presented in Figure 2. The vibration boundary Γ_v assuming a loudspeaker has a vibration velocity of $v_n = 1.0\,m/s$. The speed of sound $c_0 = 340.0\,m/s$ and air density $\rho_0 = 1.205\,kg/m^3$ were assumed.

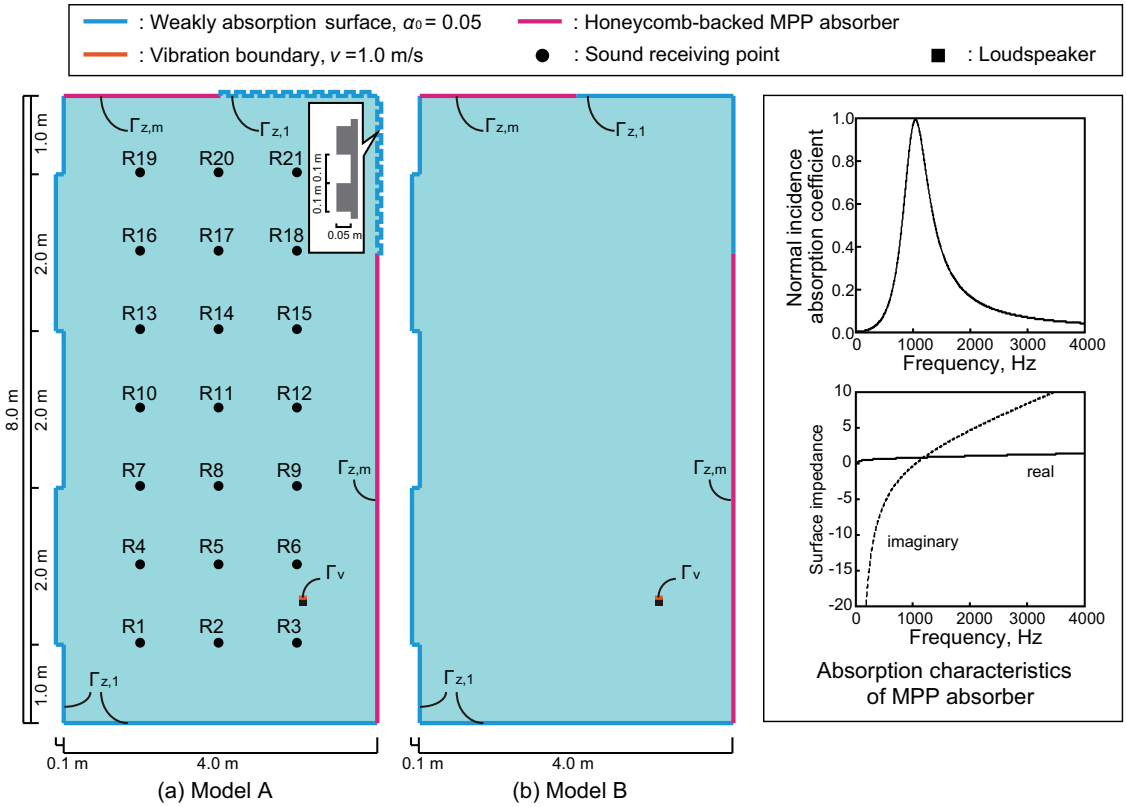

Figure 2. Two office room models with 21 sound-receiving points: (**a**) office room with the rib-type acoustic diffuser (Model A) and (**b**) more simply shaped office room without the acoustic diffuser (Model B). The room model includes three BCs: weakly absorbing surface $\Gamma_{z,1}$, frequency-dependent absorbing surface $\Gamma_{z,m}$ assuming a honeycomb-backed MPP sound absorber, and vibration boundary Γ_v assuming a loudspeaker. The absorption characteristics of the MPP absorber are also shown.

These problems have no analytical solutions. Therefore, we calculated reference solutions with a fourth-order-accurate FEM [8,52] using sufficiently fine meshes. Three meshes were created according to the analyzed frequencies where 0.01 m square elements were used for frequencies of 20 Hz to 1.5 kHz, 0.005 m square elements were used for frequencies of 1.5 kHz to 3 kHz, and 0.0025 m square elements were used for frequencies of 3 kHz to 4 kHz. These meshes have spatial resolutions of 22, 22, and 34 elements per wavelength, respectively, at 1.5 kHz, 3 kHz, and 4 kHz. Table 1 presents detailed

information of the three meshes for Model A and Model B. Here, N_{element}, N_{node}, and h respectively represent the number of elements and nodes and the element length.

Table 1. Detailed information of the used meshes for the reference solution.

	Model A			Model B		
	20 Hz–1.5 kHz	**1.5–3 kHz**	**3–4 kHz**	**20 Hz–1.5 kHz**	**1.5–3 kHz**	**3–4 kHz**
N_{element}	324,900	1,299,600	5,198,400	323,900	1,295,600	5,182,400
N_{node}	326,240	1,302,280	5,203,760	325,140	1,298,080	5,187,360
h	0.01 m	0.005 m	0.0025 m	0.01 m	0.005 m	0.0025 m
n_{w}	0.0006–0.044	0.022–0.044	0.022–0.029	0.0006–0.044	0.022–0.044	0.022–0.029

Figure 3a,c respectively shows three PW-FEM meshes of Model A with different spacial resolutions: Mesh 1, Mesh 2, and Mesh 3. Table 2 presents detailed information of the meshes which were used. Mesh 1–Mesh 3 are discretized, respectively, with rectangular elements of 0.05–0.5 m, 0.05–0.25 m, and 0.05–0.1 m. We also used three PW-FEM meshes for Model B with different spatial resolutions: Mesh 1, Mesh 2, and Mesh 3 respectively have the same spatial resolution as in Model A. Their longest element lengths in Mesh 1–Mesh 3 are respectively 5.88-, 2.94-, and 1.18-times longer than the wavelength at 4 kHz, as might be apparent in the n_{w} values in Table 2. The maxima of $h^{\Omega}_{\text{max},i}$ in Mesh 1 and Mesh 2 are respectively five-times and two-and-a-half-times longer than the minima. $h^{\Omega}_{\text{max},i}$ in Mesh 3 is constant as 0.1 m. One can find that the three PW-FEM meshes have markedly small numbers of N_{element} and N_{node} because of the use of larger elements than the wavelength of the upper-limit frequency.

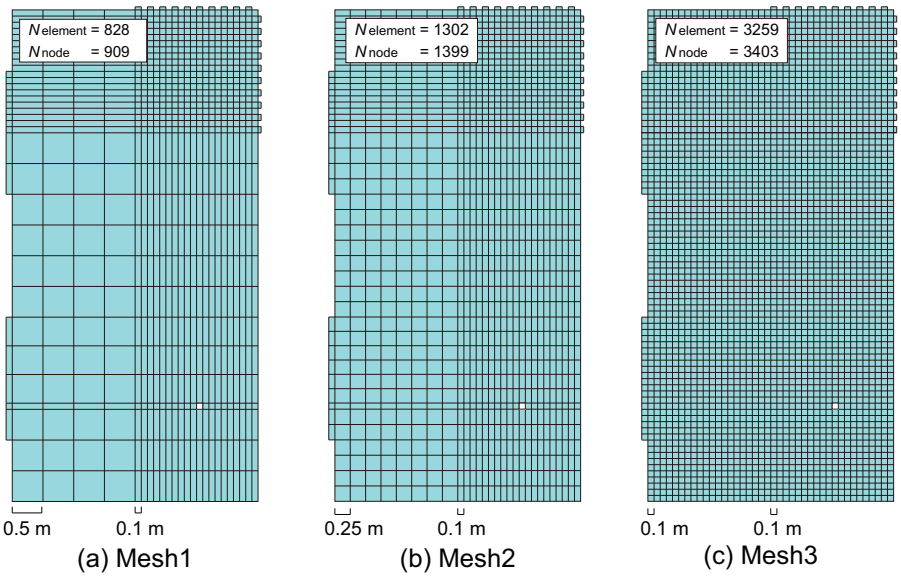

Figure 3. Meshes of Model A used for the PW-FEM: (**a**) Mesh 1, (**b**) Mesh 2, and (**c**) Mesh 3.

Table 2. Detailed information of the used meshes for the PW-FE analysis.

	Model A			Model B		
	Mesh 1	**Mesh 2**	**Mesh 3**	**Mesh 1**	**Mesh 2**	**Mesh 3**
N_{element}	828	1302	3259	808	1282	3239
N_{node}	909	1399	3403	869	1359	3363
$\Omega_{\text{max},i}$	0.1–0.5 m	0.1–0.25 m	0.1 m	0.1–0.5 m	0.1–0.25 m	0.1 m
n_{w}	0.006–5.88	0.006–2.94	0.006–1.18	0.006–5.88	0.006–2.94	0.006–1.18

In Section 3.4, to demonstrate the performance of the PW-FEM against the classical linear and quadratic FEMs, we used the office room problem with Model A, in which the classical linear FEM uses the same meshes as used for the fourth-order-accurate FEM. For the quadratic FEM, we used two meshes discretized with 0.025 m square elements at frequencies of 20 Hz to 2 kHz and with 0.0125 m square elements at frequencies of 2 kHz to 4 kHz. Table 3 presents detailed information of the meshes. Both spatial resolutions were 6.8 elements per wavelength at each upper-limit frequency.

Table 3. Detailed information of the used meshes for the quadratic FE analysis.

	Model A	
	20 Hz–2 kHz	**2–4 kHz**
N_{element}	51,984	207,936
N_{node}	209,008	833,888
h	0.025 m	0.0125 m
n_{w}	0.001–0.15	0.074–0.15

To evaluate the accuracy, we define the absolute error $L_{\text{abs}}(f)$ with respect to the spatial distribution of the sound pressure level (SPL) as:

$$L_{\text{abs}}(f) = \frac{1}{N_{\text{p}}} \sum_{i=1}^{N_{\text{p}}} |L_{\text{fem}}(f,i) - L_{\text{ref}}(f,i)|, \tag{23}$$

where $L_{\text{fem}}(f,i)$ and $L_{\text{ref}}(f,i)$ respectively represent the SPLs in a receiver i at a frequency f calculated using the PW-FEM and the classical linear and quadratic FEMs, and the reference solutions calculated using the forth-order-accurate FEM. Also, N_{p} is the number of receiving points.

3.2. Effectiveness of the Variable q-Approach against the Constant q-Approach

This section presents our demonstration of PW-FEM performance with Variable q-approach against that with the Constant q-approach through numerical experiments predicting sound fields with Model A at frequencies 20 Hz–4 kHz with a 1 Hz interval. For Mesh 3, the same results were obtained using either the Variable q-approach or the Constant q-approach because both h^{Ω}_{max} in Equation (21) and $h^{\Omega}_{\text{max},i}$ in Equation (22) are set to 0.1 m. The constant C in Equations (21) and (22) was set as eight. We can draw the same conclusion presented later for other values of C. In the present case, the DOFs in the Constant q-approach and the Variable q-approach respectively changed as 4545–58,176 and 3645–39,534 for Mesh 1, 5596–55,960 and 5146–48,056 for Mesh 2, and 10,209–78,269 for Mesh 3.

Figure 4a,c respectively portrays the comparison of the frequency responses at a receiving point R1 among the PW-FEM results calculated using the Variable q-approach and the Constant q-approach and the reference solution for Mesh 1, Mesh 2, and Mesh 3. The result obtained using the Constant q-approach with Mesh 1 presents a marked difference at higher frequencies than 500 Hz, where SPLs diverge completely from the reference solution because adding many more plane waves than necessary produce an ill-conditioned linear system. For Mesh 1, more plane waves than necessary are added to small elements because q_i are determined by the maximum edge length in all elements. The result obtained using the Variable q-approach with Mesh 1 shows a much better agreement with the reference solution at frequencies lower than 2 kHz, but still shows SPL divergence at many frequencies above 2 kHz. The results with Mesh 2 obtained using either the Variable or Constant q-approach show better agreements to the reference solution. However, the Constant q-approach has still diverged SPLs at frequencies higher than 2.5 kHz, whereas the Variable q-approach results show an excellent agreement up to 4 kHz. The results indicate that the greater the variation in the element size in a PW-FE mesh, i.e., a mesh

consisted of largely different sizes of elements, the two approaches become unstable, but the Variable q-approach can produce more stable results for such a condition to some degree. As might be apparent in the Mesh 2 and Mesh 3 results, the PW-FEM can produce an excellent agreement when using a mesh that has smaller variation in the element sizes.

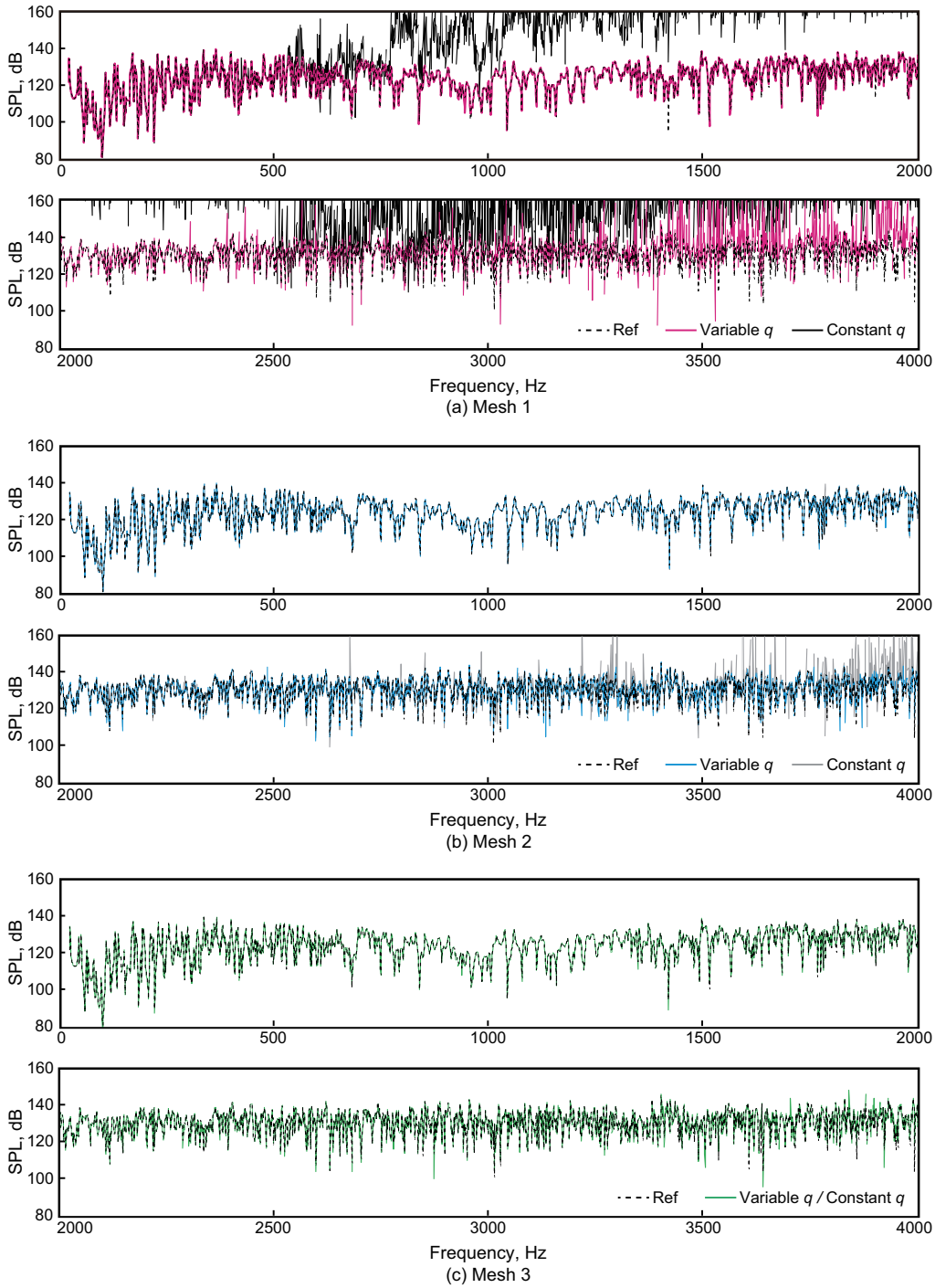

Figure 4. Comparisons of the frequency responses at R1 among the PW-FEM using the Variable q-approach and the Constant q-approach and the reference solution: (**a**) Mesh 1, (**b**) Mesh 2, and (**c**) Mesh 3.

Furthermore, Figure 5a,c portrays the spatial distributions of SPLs at 1 kHz for the reference solution and the PW-FEM using the Constant q-approach and the Variable q-approach with Mesh 1. The SPLs in the PW-FEM were calculated at the same nodes in the

reference solution. The figure includes the DOFs and absolute error $L_{\mathrm{abs}}(f)$ for the two approaches. The Constant q-approach result shows a marked difference from the reference solution with an L_{abs} of 9.2 dB. That is readily apparent where SPLs show high values. In contrast, the Variable q-approach result shows an excellent match with the reference SPL distribution with an L_{abs} of 0.1 dB. As a reference, Constant q-approach adds 26 plane waves to all nodal points, but the Variable q-approach adds 26 plane waves to nodes with $h^{\Omega}_{\mathrm{max},i}$ of 0.5 m and 12 plane waves to nodes with $h^{\Omega}_{\mathrm{max},i}$ of 0.1 m according to the value of $h^{\Omega}_{\mathrm{max},i}$.

As a quantitative evaluation of the accuracy, Figure 6 presents a comparison of the absolute errors among PW-FEMs using the Variable q-approach and the Constant q-approach for the cases with Mesh 1, Mesh 2 and Mesh 3. We calculated the absolute error using the 21 sound-receiving points shown in Figure 2. As described before, the Mesh 3 result becomes the same for the Variable and Constant q-approaches. To capture the error behavior easily, we applied 1/3 octave band averaging to the absolute error. The Constant q-approach result with Mesh 1 shows absolute errors larger than 5 dB at frequencies higher than 630 Hz. In contrast, the absolute errors using the Variable q-approach with Mesh 1 are less than 1 dB up to 2.5 kHz. However, the accuracy deteriorates at further high frequencies: 3 dB at 3.15 kHz and 7 dB at 4 kHz. The absolute errors of both approaches with Mesh 2 become much smaller compared to the Mesh 1 results, and the Variable q-approach shows better result. The absolute errors are lower than 0.4 dB up to 2.5 kHz for both approaches. At higher frequencies, the Constant q-approach has an absolute error of 3 dB at 3.15 kHz and 5 dB at 4 kHz, whereas the Variable q-approach shows absolute errors lower than 1.3 dB up to 4 kHz. Furthermore, the absolute error of the Variable q-approach with Mesh 2 is equivalent to the error with the finest mesh, Mesh 3. Because practical room acoustic problems with complex room geometries require the use of a mesh that includes various sizes of elements, q-refinement using the Variable q-approach is expected to be favorable for a robust room acoustics simulation. The next section further explores details of how mesh size and room geometry affect the robustness of the PW-FEM using the Variable q-approach.

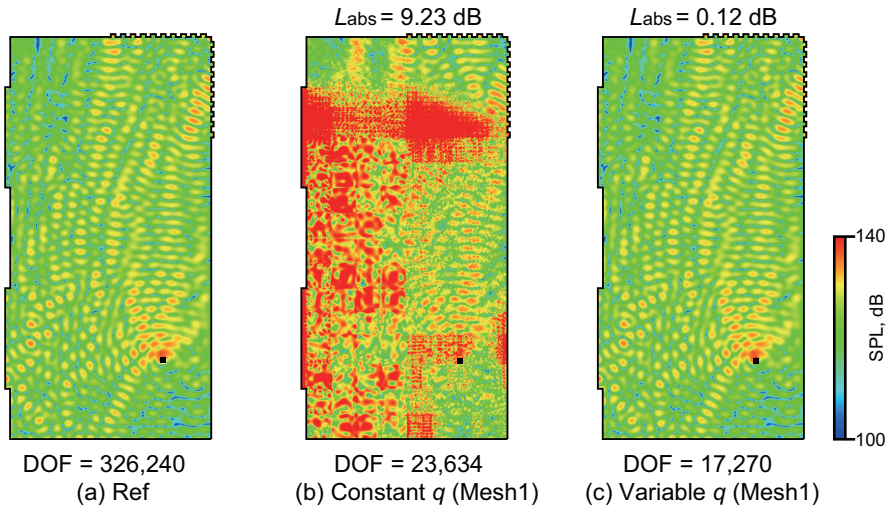

Figure 5. A comparison of the SPL distribution at 1 kHz among (**a**) the reference solution, (**b**) the PW-FEM using the Constant q-approach, and (**c**) the PW-FEM using the Variable q-approach.

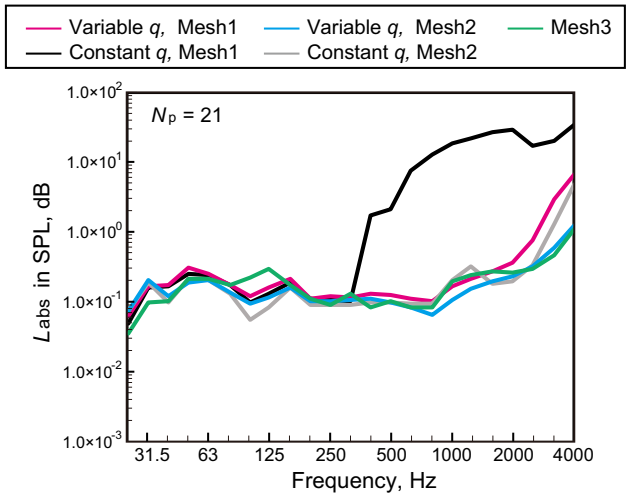

Figure 6. A comparison of the absolute errors using the Variable q-approach and the Constant q-approach.

3.3. Mesh and Room Geometry Effects on the Robustness of the PW-FEM Using the Variable q-Approach

This section presents a description of the effects of the used mesh and room geometry on the robustness of the PW-FEM using the Variable q-approach via numerical experiments predicting sound fields in the two office rooms, Model A and Model B, having different room geometries, respectively, with and without acoustic diffusers. We used the three meshes, i.e., Mesh 1–Mesh 3, having different spatial resolutions. For both room models, we calculated the sound fields at frequencies of 63 Hz, 125 Hz, 250 Hz, 500 Hz, 1 kHz, 2 kHz, 3 kHz and 4 kHz, changing the constant C in Equation (22), which controls the added plane-wave number in the plane-wave enrichment. The accuracy was evaluated using absolute error $L_{\mathrm{abs}}(f)$ at all points that correspond to all nodal points in the reference solution meshes.

Figure 7a,h shows the absolute error $L_{\mathrm{abs}}(f)$ for Model A and Model B as a function of C at the eight frequencies, as calculated using Mesh 1, Mesh 2, and Mesh 3. From these figures, one can confirm how the meshes used and room geometry affect the robustness of the PW-FEM analysis when using the different values of C. The figures show different error behaviors for the results below 500 Hz and above 1 kHz. Below 500 Hz, where the wavelength is still larger than the element sizes for all meshes, the absolute errors tend to become smaller as C increases regardless of the used meshes and models. In addition, the error magnitude is smaller than 1 dB. In contrast, at frequencies higher than 1 kHz, one can clearly found the effects of the mesh used and room geometry on the robustness of the PW-FEM. First, regarding the room geometry effect, larger absolute errors can be seen for the more complex model, Model A, including the acoustic diffuser, when the errors are compared with the same spatial resolution mesh. Furthermore, one can find for the Model A that the range of C keeps the absolute error small becoming narrower than Model B. For example, at 1 kHz, the absolute error of Model A with Mesh 1 remains less than 1 dB for the C values up to nine, but that of Model B keeps the error level for all C's up to thirteen. This narrow band effect in C is also true for both models when using a mesh including larger-sized elements. For Model A at 2 kHz, we can find that the absolute errors in Mesh 1 show less than 1 dB for C = 6–8, but for Mesh 2 and Mesh 3, the ranges that keep the error level become respectively C = 5–10 and C = 6–13. For Mesh 1 in Model B at 2 kHz, the small error level can be achieved with C = 5–8 and 10, but Mesh 2 and Mesh 3 achieve this for any C values. At the highest 4 kHz, the absolute errors of Model A using the coarsest Mesh 1 no longer become less than 1 dB for any values of C, whereas Model B using Mesh 1 can achieve the small error level with C = 10–13. However, for Model A, the error can reduce within 1 dB using the finer Mesh 2 and Mesh 3 when using appropriate values of C. For Mesh 2, C = 8 and 9 only achieve this small error level. As a

reference, Figure 8a,c shows a comparison of the spatial distributions of the SPLs for Model A among the reference solution, the PW-FEM using Mesh 2 with C = 9, and the PW-FEM using Mesh 2 with C = 11. The figure also includes a spatial distribution of the absolute error between the reference solution and the PW-FEM results. The SPL distributions from the PW-FEM using Mesh 2 with C = 9 show an excellent agreement with the reference solution with L_{abs} = 0.4 dB, whereas the large error of L_{abs} = 4.8 dB can be found in the SPL distributions from the PW-FEM using Mesh 2 with C = 11. For Mesh 3, that keeps the maximum element size, comparable to the wavelength of the upper-limit frequency, we can use a wider range of C = 8 and 10–13. From these results, it can be concluded that (1) the robustness of the PW-FEM on 2D room acoustic problems depends on both the used mesh and room geometry, especially at high frequencies; (2) using a coarse mesh including an element size larger than the wavelength of the upper-limit frequency makes it challenging to set an appropriate value of C especially for complex room shapes; (3) the difficulty can be alleviated using a mesh where the maximum element size remains comparable to the wavelength of the upper-limit frequency.

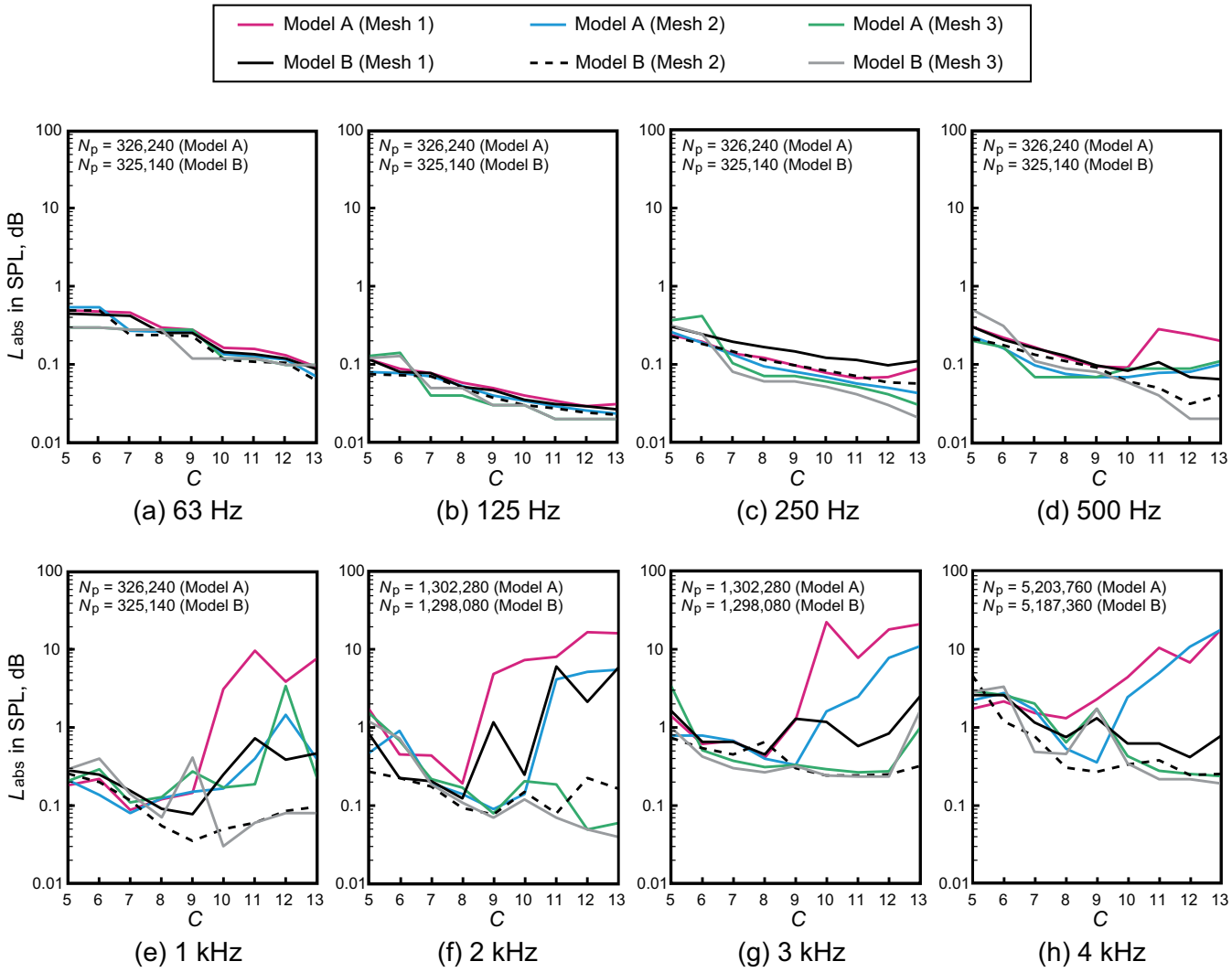

Figure 7. Comparisons of the absolute errors at eight frequencies as a function of C for Model A and Model B with three meshes, Mesh 1–Mesh 3: (**a**) 63 Hz, (**b**) 125 Hz, (**c**) 250 Hz, (**d**) 500 Hz, (**e**) 1 kHz, (**f**) 2 kHz, (**g**) 3 kHz, and (**h**) 4 kHz.

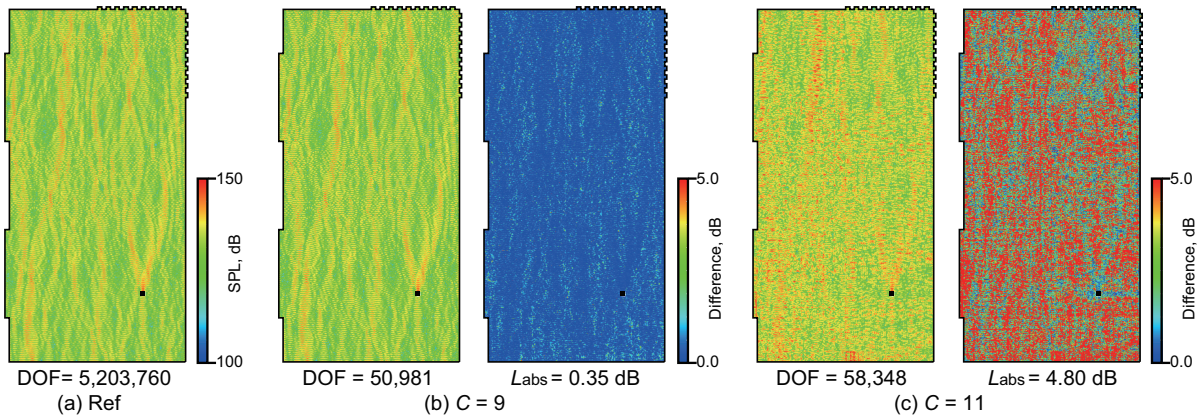

Figure 8. A comparison of the SPL distribution at 4 kHz of the reference solution and the PW-FEM using Mesh 2 with $C = 9$ and $C = 11$ and the SPL difference from the reference solution.

3.4. Performance Comparison with Classical Linear and Quadratic FEMs

We demonstrate the accuracy and computational costs of the PW-FEM on 2D room acoustic problems against the classical and quadratic FEMs through numerical experiments predicting the sound field in Model A at frequencies of 20 Hz to 4 kHz with a 1 Hz interval. The PW-FEM uses the recently developed rule for determining integration points number. Both the PW-FEM and the classical FEMs use a sparse direct solver, PARDISO, for the linear system solution. We used the three meshes shown in Figure 3a,c, with the constant C set to eight for the PW-FE analyses. For the linear and the quadratic FEMs respectively using Q4s and Q9s as the FEs, we used three meshes in Tables 1 and two meshes in Table 3. All computations were performed with a computer, PRIMERGY CX2550/CX2560 M4 with two processors (Xeon Gold 6154 3.0 GHz, 18 core; Intel Corp., Santa Clara, CA, USA) using a Fortran compiler (Ver. 2020; Intel Corp.). Note that the computational cost comparison was based on sequential computation.

As a comparison of the accuracy, Figure 9 shows the absolute errors among the PW-FEMs using the three meshes, the linear FEM, and the quadratic FEM at frequencies up to 4 kHz. Only the PW-FEMs using Mesh 2 and Mesh 3 show a high accuracy at all frequencies. The PW-FEMs using Mesh 2 have absolute errors less than 1 dB at frequencies below 3.15 kHz and 1.3 dB at 4 kHz, and the same level of accuracy can also be seen for the PW-FEMs using Mesh 3. In contrast, the PW-FEM using Mesh 1 shows higher errors 3 dB at 3.15 kHz and 7 dB at 4 kHz. The classical linear and quadratic FEMs have higher accuracy compared to the PW-FEMs at frequencies below 250 Hz, but have larger errors at frequencies greater than 250 Hz because of the large dispersion errors. The linear FEM shows absolute errors higher than 3 dB at frequencies above 1.25 kHz. The quadratic FEM also has absolute errors higher than 3 dB at frequencies above 3.15 kHz. The results clearly demonstrate that the PW-FEM using an appropriate mesh and C value produces highly accurate results at wideband compared to the classical linear and quadratic FEMs, which use higher-resolution meshes than the well-known rule of thumb, on 2D room acoustics problems.

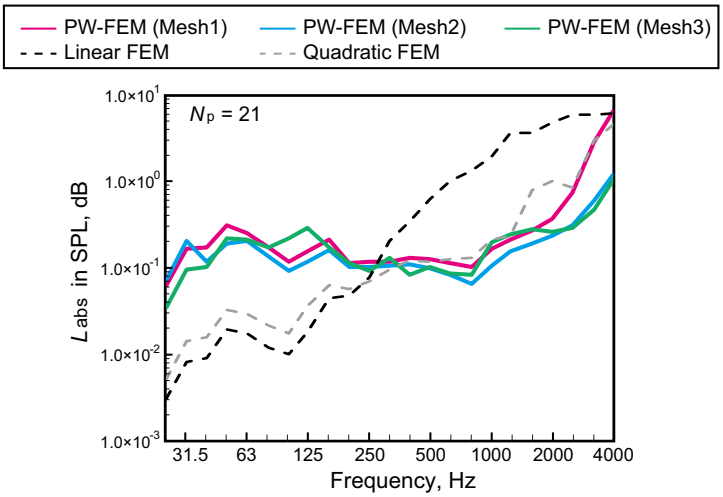

Figure 9. A comparison of the absolute errors of the PW-FEM using Mesh 1, Mesh 2, and Mesh 3 and the classical linear and quadratic FEMs.

In room acoustics simulation, the calculation of an impulse response is essential to evaluate the room acoustics. To this point, we can further demonstrate the superior approximation capability of the PW-FEM against the quadratic FEM. Figure 10a,d shows a comparison of the impulse responses calculated using the inverse Fourier transform of the reference solution and the PW-FEM using Mesh 3 and the quadratic FEM at time ranges t = 0.0–0.02 s and 0.30–0.32 s. We considered the modulated Gaussian pulse waveform with the frequency characteristics in Figure 11 for the inverse Fourier transform. The source function form $v(t)$ is defined as:

$$v(t) = \frac{2\pi}{\rho_0}(0.4 - c_0 t)\mathrm{e}^{\frac{-(0.4-c_0 t)^2}{d^2}}, \tag{24}$$

where the parameter d is defined as $d = \frac{c_0 \mathrm{e}}{2\pi f_{\max}}$ with the upper-limit frequency $f_{\max}$ = 2800 Hz. Furthermore, we re-computed the complex sound pressure at frequencies of 1 Hz to 6 kHz with a 1 Hz interval to guarantee spectrum continuity in the inverse Fourier transform. From Figure 10a,c, we can see that both the PW-FEM and quadratic FEM show excellent agreement to the reference solution at the early time region at t = 0.0–0.02 s. However, the quadratic FEM shows a large discrepancy from the reference solution at t = 0.3–0.32 s, whereas the PW-FEM still shows excellent agreement. This indicates that waveforms calculated using the quadratic FEM deteriorate over time with its dispersion error characteristics, i.e., the sound speed increases beyond the exact sound speed at higher frequencies. To quantitatively evaluate the similarity to the reference solution waveforms, we define the cross-correlation coefficient as:

$$CC = \frac{\sum_{n=1}^{N_{\text{step}}} \tilde{p}^n p_{\text{ref}}^n}{\sqrt{\sum_{n=1}^{N_{\text{step}}} (\tilde{p}^n)^2}\sqrt{\sum_{n=1}^{N_{\text{step}}} (p_{\text{ref}}^n)^2}}, \tag{25}$$

where $\tilde{p}^n$ and p_{ref}^n respectively represent the sound pressure at time step n calculated using the PW-FEM or quadratic FEM and the reference solution. N_{step} denotes the number of time steps. The PW-FEM waveforms showed a higher CC value averaged over 21 receiving points with CC = 0.998, whereas the quadratic FEM has a slightly lower CC value of 0.960.

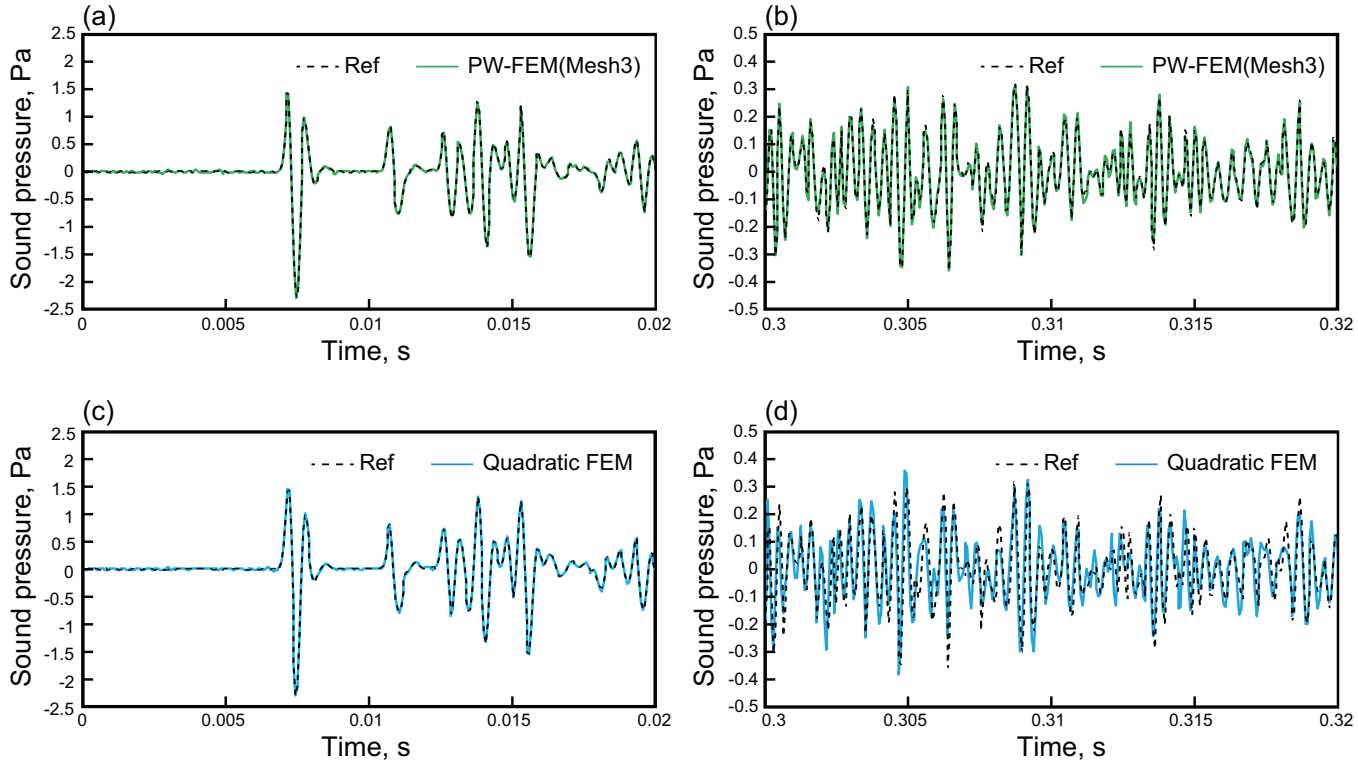

Figure 10. Comparisons of the waveforms at R1 between (**a**) the reference solution (Ref) and the PW-FEM (Mesh 3) at time t = 0–0.02 s, (**b**) the Ref and the PW-FEM (Mesh 3) at time t = 0.3–0.32 s, (**c**) the Ref and the quadratic FEM at time t = 0–0.02 s, and (**d**) the Ref and the quadratic FEM at time t = 0.3–0.32 s.

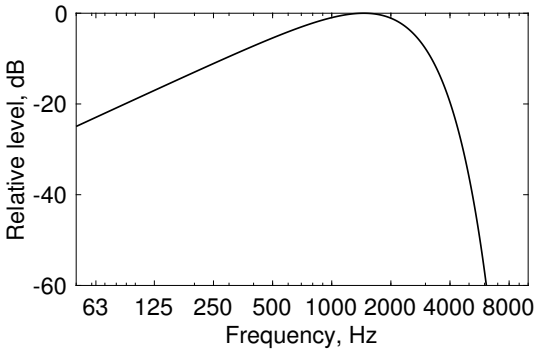

Figure 11. Frequency characteristics of the modulated Gaussian pulse.

Figure 12a,c presents the comparisons of the CPU times on sequential calculation of the PW-FEMs with Mesh 1, Mesh 2 and Mesh 3 and the classical linear and quadratic FEMs, respectively, showing (a) CPU times in constructing the global stiffness and mass matrix, $\boldsymbol{K}$ and $\boldsymbol{M}$, (b) CPU times in solving the linear system of equations, and (c) CPU times in total. The results indicate that the hotspot of computations in the PW-FEM is the global stiffness and mass matrix construction process, which occupy 96.4% in the total CPU time for Mesh 1 at 4 kHz, and it is 82.6% for Mesh 2 and 61.7% for Mesh 3. It is also noteworthy that using the finest mesh, Mesh 3, provides the fastest analysis at frequencies higher than 1.5 kHz. In contrast, the PW-FEM can quickly solve the linear system of equations with the sparse direct solver thanks to the marked reduction in the DOFs, as shown in Figure 12b. As an example, the total CPU times at 4 kHz are 191 s (Mesh 1), 44 s (Mesh 2), and 21 s (Mesh 3). In the PW-FEM used here, the element stiffness and mass matrix of size $q_{\mathrm{tot}}^{\Omega_{\mathrm{e}}} \times q_{\mathrm{tot}}^{\Omega_{\mathrm{e}}}$ must be processed by the high-order Gauss–Legendre integration, which has an $\mathcal{O}(n_{\mathrm{g}}^2)$ numerical complexity. Since the integration point number n_{g} increases as

the element size becomes larger, the computational cost per element at high frequencies increases significantly, as can be seen in the Mesh 1 result. In addition, the contribution of increasing n_g is larger than that of increasing elements by using small-sized elements. Therefore, the total CPU time becomes shorter for the case using a mesh with smaller elements, as can be seen in Figure 12c. This result and considering the robustness issue suggest the use of a mesh discretized with an element size comparable to the wavelength of the upper-limit frequency to perform efficient acoustics simulation with the PW-FEM when using a high-order Gauss–Legendre rule.

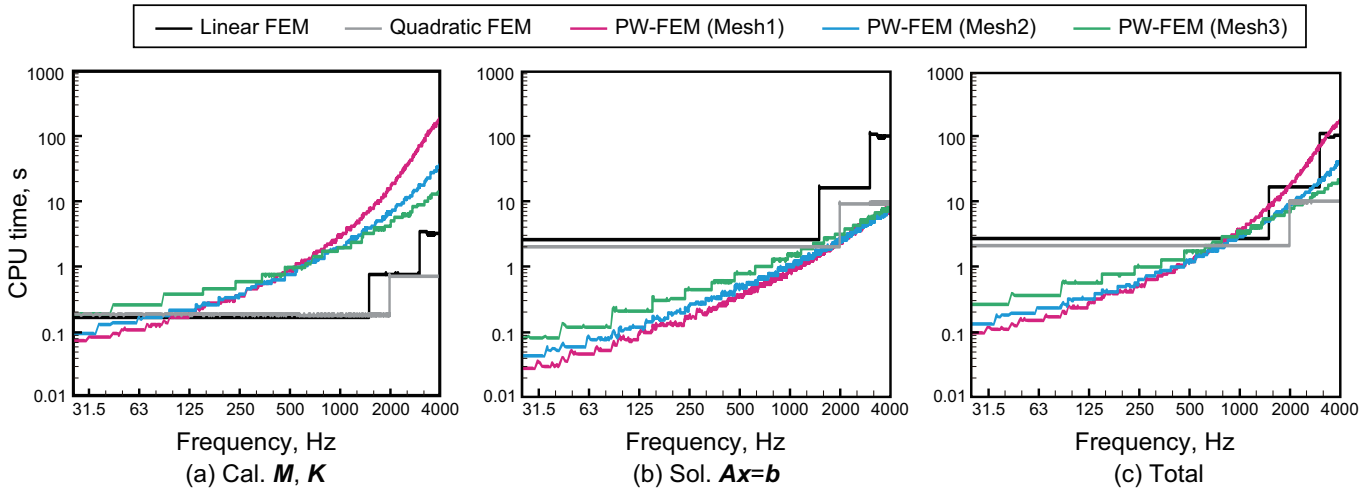

Figure 12. Comparisons of the CPU times on sequential calculation of the PW-FEM with Mesh 1, Mesh 2, and Mesh 3 and the classical linear and quadratic FEMs: (**a**) CPU times in constructing the global stiffness and mass matrix, $\boldsymbol{K}$ and $\boldsymbol{M}$, (**b**) CPU times in solving the linear system of equations, and (**c**) CPU times in total.

However, the classical linear and quadratic FEMs can construct element matrices significantly faster than the PW-FEM, even in meshes including a significantly large number of FEs, as can be seen in Figure 12a. Such faster matrices are possible because the linear and quadratic FEMs respectively need only an $\mathcal{O}(1)$ numerical complexity for element construction in the stiffness and mass matrix of size 4×4 and 9×9 using two- and three-point Gauss–Legendre integrations. However, the classical linear and quadratic FEMs have huge linear system sizes with DOFs greater than 5,000,000 for the linear FEM and 800,000 for the quadratic FEM, as can be seen in the used mesh at 4 kHz. Therefore, the hotspots of computation in the linear and quadratic FEMs are the solution process of the linear system solution, as shown in Figure 12b. The linear system solution process respectively occupies 97.0% and 93.3% of all CPU time for the linear and quadratic FEMs at 4 kHz. Results of the computational times' comparison among the three solvers show that, at 4 kHz, the PW-FEM using Mesh 3 is five-times faster than the linear FEM and two-times slower than the quadratic FEM. The quadratic FEM is the fastest, but the PW-FEM using Mesh 3 has a much better accuracy, as shown in Figure 9, and with a higher CC value in the impulse response.

To compare the memory requirements of the three solvers, Figure 13a,c presents comparisons of (a) the DOFs, (b) the number of nonzero elements in the coefficient matrix, and (c) the peak memory consumption at frequencies up to 4 kHz. As shown in Figure 13a, the DOFs in the PW-FEM using the three meshes respectively change as 3645–39,534 for Mesh 1, 5146–48,056 for Mesh 2, and 10,209–78,269 for Mesh 3. The linear FEM needs DOFs of 326,240, 1,302,280, and 5,203,760 for the analyses at frequencies of 20 Hz to 1.5 kHz, 1.5 kHz to 3 kHz, and 3 kHz to 4 kHz. For the quadratic FEM, 209,008 DOFs and 833,888 DOFs are required at frequencies of 20 Hz to 2 kHz and 2 kHz to 4 kHz. This comparison suggests that the PW-FEM with Mesh 3 has much better accuracy than the

classical FEMs, requiring DOFs of less than 1/67 and 1/11 compared to the classical linear and quadratic FEMs.

Furthermore, Figure 13b shows that the numbers of nonzero elements in the coefficient matrix of the PW-FEM are about 1/3 of the linear FEM and almost identical to the quadratic FEM at 4 kHz. Results of comparison of the DOFs and the number of nonzero elements also show that the PW-FEM matrix is sparse, where the nonzero elements appear in only 1.1% (Mesh 1), 0.7% (Mesh 2), and 0.3% (Mesh 3) components in the coefficient matrix, i.e., 99% of matrix components are zero. With this sparsity, the PW-FEM using the three meshes requires 1.7GB (Mesh 1), 1.7GB (Mesh 2), and 2GB (Mesh 3) at 4 kHz. Although the PW-FEM has much better accuracy, these memory requirements are lower than the linear and quadratic FEMs, which respectively require 15.8 GB and 2.3 GB at 4 kHz. It can be concluded that the PW-FEM is a memory-efficient method able to obtain accurate results at wide frequencies.

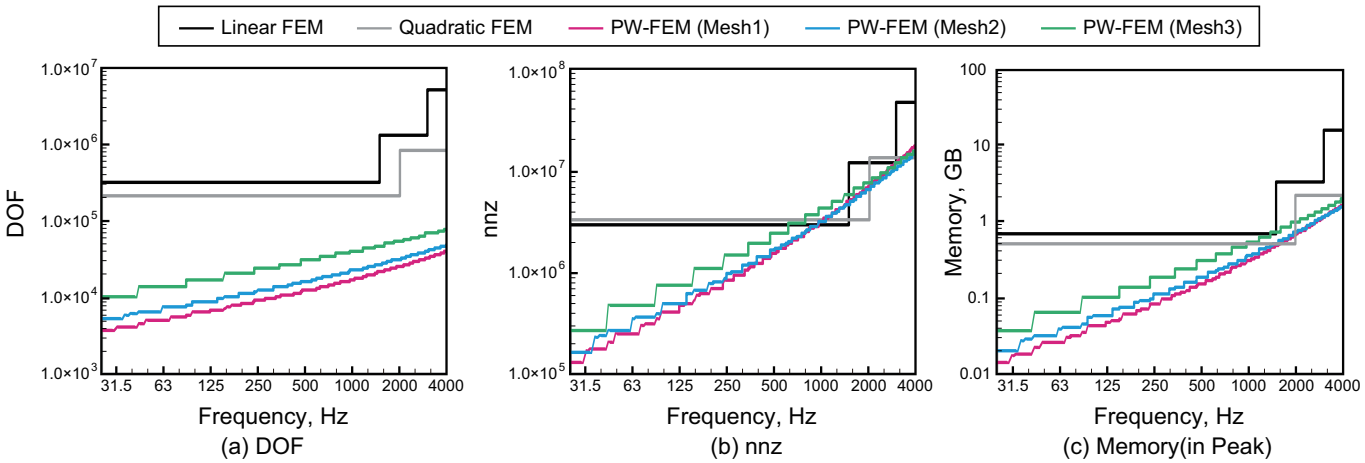

Figure 13. Comparisons of (**a**) the DOFs, (**b**) the number of nonzero elements, and (**c**) the peak memory consumption, of the PW-FEM with Mesh 1, Mesh 2, and Mesh 3 and the classical linear and quadratic FEMs.

4. Conclusions

This paper has presented a discussion of the robustness of the PW-FEM on 2D room acoustic problems, specifically addressing the effects of the spatial resolution of the mesh that is used and room geometry. The discussion includes a suggestion on the mesh generation for robust and efficient simulations when using a high-order Gauss–Legendre rule in the element matrix calculations. We also demonstrated the performance of the PW-FEM using our recently developed rule for determining the integration points number in a high-order Gauss–Legendre rule and a sparse direct solver against the classical linear and quadratic FEMs. For the discussion of the robustness and the performance examination against the two classical FEMs, sound fields in real-scale office rooms with and without rib-type acoustic diffusers were computed at frequencies up to 4 kHz. First, we demonstrated the effectiveness of using q-refinement with the Variable q-approach over the Constant q-approach since the Variable q-approach can produce more stable results when a mesh includes elements of various sizes, which is a natural situation in the room acoustics problem. Then, we examined how the robustness of the PW-FEM changes according to the spatial resolution of the used meshes and the complexity of the room geometry. The results revealed that the robustness of the PW-FEM is dependent on both the spatial resolution of the meshes used and the complexity of the room geometry, especially for a high-frequency range. Use of coarse meshes including elements that have a larger size than the wavelength of the upper-limit frequency makes the setup of an appropriate value of C considerably difficult, especially for complex room shapes, because the range of C which maintains a small error level becomes narrow. However, we found that the difficulty can be alleviated

when using a mesh in which the maximum element size maintains a comparable value to the wavelength of the upper-limit frequency. In that case, we have a wider range of C to keep the error level small. Therefore, from these results, as the novelty of the present work, we can make a suggestion using a mesh discretized with element sizes comparable to the wavelength of the upper-limit frequency for a robust room acoustics simulation using the PW-FEM, i.e., n_{w} should be kept as $n_{\mathrm{w}} \simeq 1$. The proposal is effective from the aspect of computational efficiency. As demonstrated in the performance examination, the computational times of the PW-FEM using a high-order Gauss–Legendre rule become shorter with a fine mesh. Additionally, we still have a sufficient DOF reduction while keeping a high accuracy even in the use of the fine mesh discretized with element sizes comparable to the wavelength of the upper-limit frequency. Because of the DOF reduction and the sparsity of coefficient matrix, we can say that the PW-FEM is a memory-efficient solver for wideband room acoustics simulation. The performance examination further revealed that the PW-FEM using our recently developed rule for determining n_{g} and a sparse direct solver showed much better accuracy with smaller memory than the classical linear and quadratic FEMs at the wideband and at a longer time range, but still with two-times slower computational time as the quadratic FEM, which uses a mesh with a spatial resolution of 6.8 elements per wavelength.

However, future studies must be undertaken to elucidate characteristics of the PW-FEM on room acoustic problems. Our future studies will include the application of the present PW-FEM with the suggestion for larger-sized rooms with more complex geometries such as concert halls. Also, we will develop a robust 3D room acoustic solver using PW-FEM. Regarding this point, the present formulation with the recently developed integration rules and the proposal on mesh generation would be helpful for 3D analysis with the definition of plane waves in the spherical coordinate system because the element matrices construction process in 3D problems is more time consuming than 2D problems. Furthermore, the proposal on mesh generation will be a good basis for establishing a robust parameter setup for 3D room acoustics simulation.

Author Contributions: Conceptualization, T.O.; formal analysis, S.M.; funding acquisition, T.O.; investigation, S.M.; methodology, S.M. and T.O.; supervision, T.O.; project administration, K.S.; resources, T.O.; software, S.M.; supervision, T.O.; validation, S.M.; visualization, S.M.; writing—original draft, S.M. and T.O.; writing—review and editing, S.M., T.O. and K.S. All authors have read and agreed to the published version of the manuscript.

Funding: This work was supported in part by JSPS KAKENHI Grant No. 20K04806.

Institutional Review Board Statement: Not applicable.

Informed Consent Statement: Not applicable.

Data Availability Statement: Not applicable.

Acknowledgments: The computation was partly carried out using the computer resources offered by the Research Institute for Information Technology, Kyushu University.

Conflicts of Interest: The authors declare no conflict of interest.

References

1. Savioja, L.; Svensson, U.P. Overview of geometrical room acoustic modeling techniques. *J. Acous. Soc. Am.* **2015**, *138*, 708–730. [CrossRef]
2. Sakuma, T.; Sakamoto, S.; Otsuru, T. (Eds.) *Computational Simulation in Architectural and Environmental Acoustics—Methods and Applications of Wave-Based Computation*; Springer: Tokyo, Japan, 2014.
3. Okuzono, T.; Otsuru, T.; Tomiku, R.; Okamoto, N. A finite element method using dispersion reduced spline elements for room acoustics simulation. *Appl. Acoust.* **2014**, *79*, 1–8. [CrossRef]
4. Botteldooren, D. Finite-difference time-domain simulation of low-frequency room acoustics problems. *J. Acoust. Soc. Am.* **1995**, *98*, 3302–3308. [CrossRef]
5. Otsuru, T.; Okamoto, N.; Okuzono, T.; Sueyoshi, T. Applications of large-scale finite element sound field analysis onto room acoustics. In Proceedings of the 19th International Congress on Acoustics, Madrid, Spain, 2–7 September 2007.

6. Okamoto, N.; Tomiku, R.; Otsuru, T.; Yasuda, Y. Numerical analysis of large-scale sound fields using iterative methods part II: Application of Krylov subspace methods to finite element analysis. *J. Comput. Acoust.* **2007**, *15*, 473–493. [CrossRef]
7. Aretz, M.; Vorländer, M. Combined wave and ray based room acoustic simulations of audio systems in car passenger compartments, Part II: Comparison of simulations and measurements. *Appl. Acoust.* **2014**, *76*, 52–65. [CrossRef]
8. Okuzono, T.; Sakagami, K. A frequency domain finite element solver for acoustic simulations of 3D rooms with microperforated panel absorbers. *Appl. Acoust.* **2018**, *129*, 1–12. [CrossRef]
9. Hoshi, K.; Hanyu, T.; Okuozno, T.; Sakagami, K.; Yairi, M.; Harada, S.; Takahashi, S.; Ueda, Y. Implementation experiment of a honeycomb-backed MPP sound absorber in a meeting room. *Appl. Acoust.* **2020**, *157*, 107000. [CrossRef]
10. Yasuda, Y.; Ueno, S.; Kadota, M.; Sekine, H. Applicability of locally reacting boundary conditions to porous material layer backed by rigid wall: Wave-based numerical study in non-diffuse sound field with unevenly distributed sound absorbing surfaces. *Appl. Acoust.* **2016**, *113*, 45–57. [CrossRef]
11. Yasuda, Y.; Saito, K.; Sekine, H. Effects of the convergence tolerance of iterative methods used in the boundary element method on the calculation results of sound fields in rooms. *Appl. Acoust.* **2020**, *157*, 106997. [CrossRef]
12. Sakamoto, S. Phase-error analysis of high-order finite-difference time-domain scheme and its influence on calculation results of impulse response in closed sound field. *Acoust. Sci. Technol.* **2007**, *28*, 295–309. [CrossRef]
13. Kowalczyk, K.; Walstijn, M. Formulation of locally reacting surfaces in FDTD/K-DWM modelling of acoustic spaces. *Acta Acust. United Acust.* **2008**, *94*, 891–906. [CrossRef]
14. Kowalczyk, K.; Van Walstijn, M. Room Acoustics Simulation Using 3-D Compact Explicit FDTD Schemes. *IEEE Trans. Audio Speech Lang. Process.* **2010**, *19*, 4–46. [CrossRef]
15. Sakamoto, S.; Nagatomo, H.; Ushiyama, A.; Tachibana, H. Calculation of impulse responses and acoustic parameters in a hall by the finite-difference time-domain method. *Acoust. Sci. Technol.* **2008**, *29*, 256–265. [CrossRef]
16. Hamilton, B.; Bilbao, S. FDTD methods for 3-D room acoustics simulation with high-order accuracy in space and time. *IEEE Trans. Audio Speech Lang. Process.* **2017**, *25*, 2112–2124. [CrossRef]
17. Okuzono, T.; Otsuru, T.; Tomiku, R.; Okamoto, N. Fundamental accuracy of time domain finite element method for sound field analysis of rooms. *Appl. Acoust.* **2010**, *71*, 940–946. [CrossRef]
18. Okuzono, T.; Yoshida, T.; Sakagami, K.; Otsuru, T. An explicit time-domain finite element method for room acoustics simulations: Comparison of the performance with implicit methods. *Appl. Acoust.* **2015**, *104*, 76–84. [CrossRef]
19. Okuzono, T.; Shimizu, N.; Sakagami, K. Predicting absorption characteristics of single-leaf permeable membrane absorbers using finite element method in a time domain. *Appl. Acoust.* **2019**, *151*, 172–182. [CrossRef]
20. Bilbao, S. Modeling of Complex Geometries and Boundary Conditions in Finite Difference/Finite Volume Time Domain Room Acoustics Simulation. *IEEE Trans. Audio Speech Lang. Process.* **2013**, *21*, 1524–1533. [CrossRef]
21. Bilbao, S.; Hamilton, B.; Botts, J.; Savioja, L. Finite volume time domain room acoustics simulation under general impedance boundary conditions. *IEEE Trans. Audio Speech Lang. Process.* **2016**, *24*, 161–173. [CrossRef]
22. Hornikx, M.; Hak, C.; Wenmaekers, R. Acoustic modelling of sports halls, two case studies. *J. Build. Perform. Simul.* **2015**, *8*, 26–38. [CrossRef]
23. Hornikx, M.; Krijnen, T.; van Harten, L. openPTSD: The open source pseudo-spectral time-domain method for acoustic propagation. *Comput. Phys. Commun.* **2016**, *203*, 298–308. [CrossRef]
24. Simonaho, S.P.; Lähivaara, T.; Huttunen, T. Modeling of acoustic wave propagation in time-domain using the discontinuous Galerkin method—A comparison with measurements. *Appl. Acoust.* **2012**, *73*, 173–183. [CrossRef]
25. Wang, H.; Sihar, I.; Pagán, Muńoz, R.; Hornikx, M. Room acoustics modelling in the time-domain with the nodal discontinuous Galerkin method. *Acoust. Soc. Am.* **2019**, *145*, 2650–2663. [CrossRef] [PubMed]
26. Wang, H.; Hornikx, M. Time-domain impedance boundary condition modeling with the discontinuous Galerkin method for room acoustics simulations. *J. Acoust. Soc. Am.* **2020**, *147*, 2534–2546. [CrossRef] [PubMed]
27. Pind, F.; Jeong, C.H.; Hesthaven, J.S.; Engsig-Karup, A.P.; Strømann-Andersen, J. A phenomenological extended-reaction boundary model for time-domain wave-based acoustic simulations under sparse reflection conditions using a wave splitting method. *Appl. Acoust.* **2021**, *172*, 107596. [CrossRef]
28. Mehra, R.; Raghuvanshi, N.; Savioja, L.; Lin, M.C.; Manocha, D. An efficient GPU-based time domain solver for the acoustic wave equation. *Appl. Acoust.* **2012**, *73*, 83–94. [CrossRef]
29. Rabisse, K.; Ducourneau, J.; Faiz, A.; Trompette, N. Numerical modelling of sound propagation in rooms bounded by walls with rectangular irregularities and frequency-dependent impedance. *J. Sound Vib.* **2019**, *440*, 291–314. [CrossRef]
30. Melenk, J.M.; Babuška, I. Partition of unity finite element method: Basic theory and applications. *Comput. Methods Appl. Mech. Eng.* **1996**, *139*, 289–314. [CrossRef]
31. Babuška, I.; Melenk, J.M. The partition of unity method. *Int. J. Numer. Meth. Eng.* **1997**, *40*, 727–758. [CrossRef]
32. Laghrouche, O.; Mohamed, M.S. Locally enriched finite elements for the Helmholtz equation in two dimensions. *Comput. Struct.* **2010**, *88*, 469–1473. [CrossRef]
33. Mohamed, M.S.; Laghrouche, O.; El-Kacimi, A. Some numerical aspects of the PUFEM for efficient solution of 2D Helmholtz problems. *Comput. Struct.* **2010**, *88*, 1484–1491. [CrossRef]
34. Mohamed, M.S. Numerical Aspects of the PUFEM for Efficient Solution of Helmholtz Problems. Ph.D. Thesis, Heriot–Watt University, Edinburgh, UK, 2010.

35. Dinachandra, M.; Raju, S. Plane wave enriched Partition of Unity Isogeometric Analysis (PUIGA) for 2D-Helmholtz problems. *Comput. Methods Appl. Mech. Eng.* **2018**, *335*, 380–402. [CrossRef]
36. Diwan, G.C.; Mohamed, M.S. Pollution studies for high order isogeometric analysis and finite element for acoustic problems. *Comput. Methods Appl. Mech. Eng.* **2019**, *350*, 701–718. [CrossRef]
37. Okuzono, T.; Mohamed, M.S.; Sakagami, K. Potential of room acoustic solver with plane-wave-enriched finite element method. *Appl. Sci.* **2020**, *10*, 1969. [CrossRef]
38. Chazot, J.D.; Nennig, B.; Perrey-Debain, E. Performances of the partition of unity finite element method for the analysis of two-dimensional interior sound fields with absorbing materials. *J. Sound Vib.* **2013**, *332*, 1918–1929. [CrossRef]
39. Chazot, J.D.; Perrey-Debain, E. The partition of unity finite element method for the simulation of waves in air and poroelastic media. *J. Acoust. Soc. Am.* **2014**, *135*, 724–733. [CrossRef]
40. Tamaru, K.; Okuzono, T.; Mukae, S.; Sakagami, K. Exploration of efficient numerical integration rule for wide-band room-acoustics simulations by plane-wave-enriched finite-element method. *Acoust. Sci. Technol.* **2020**, *42*, 231–240. [CrossRef]
41. Hiptmair, R.; Moiola, A.; Perugia, I. Survey of Trefftz methods for the Helmholtz equation. In *Building Bridges: Connections and Challenges in Modern Approaches to Numerical Partial Differential Equations*; Springer: Cham, Switzerland, 2016; pp. 237–278.
42. Mukae, S.; Okuzono, T.; Tamaru, K.; Sakagami, K. Modeling microperforated panels and permeable membranes for a room acoustic solver with plane-wave-enriched FEM. *Appl. Acoust.* **2022**, *185*, 108383. [CrossRef]
43. Maa, D.Y. Microperforated-panel wideband absorbers. *Noise Control Eng. J.* **1987**, *29*, 77–84. [CrossRef]
44. Sakagami, K.; Funahashi, K.; Somatomo, Y.; Okuzono, T.; Nishikawa, C.; Toyoda, M. An experimental study on the absorption characteristics of a three-dimensional permeable membrane space sound absorber. *Noise Control Eng. J.* **2015**, *63*, 300–307. [CrossRef]
45. Craggs, A. A finite element model for rigid porous absorbing materials. *J. Sound Vib.* **1978**, *61*, 101–111. [CrossRef]
46. Craggs, A. Coupling of finite element acoustic absorption models. *J. Sound Vib.* **1979**, *66*, 605–613. [CrossRef]
47. Easwaran, V.; Munjal, M.L. Finite element analysis of wedges used in anechoic chambers. *J. Sound Vib.* **1993**, *160*, 333–350. [CrossRef]
48. Allard, J.F.; Atalla, N. Sound propagation in porous materials having a rigid frame. In *Propagation of Sound in Porous Media: Modeling Sound Absorbing Materials*, 2nd ed.; John Wiley & Sons, Ltd.: Chichester, UK, 2009; pp. 73–109.
49. Allard, J.F.; Atalla, N. Finite element modeling of poroelastic materials. In *Propagation of Sound in Porous Media: Modeling Sound Absorbing Materials*, 2nd ed.; John Wiley & Sons, Ltd.: Chichester, UK, 2009; pp. 309–349.
50. Bettess, P.; Shirron, J.; Laghrouche, O.; Peseux, B.; Sugimoto, R.; Trevelyan, J. A numerical integration scheme for special finite elements for the Helmholtz equation. *Int. J. Numer. Meth. Eng.* **2003**, *56*, 531–552. [CrossRef]
51. Banerjee, S.; Sukumar, N. Exact integration scheme for planewave-enriched partition of unity finite element method to solve the Helmholtz problem. *Comput. Methods Appl. Mech. Eng.* **2017**, *317*, 619–648. [CrossRef]
52. Guddati, M.N.; Yue, B. Modified integration rules for reducing dispersion error in finite element methods. *Comput. Methods Appl. Mech. Eng.* **2004**, *193*, 275–287. [CrossRef]